ACSNANO

www.acsnano.org

ARTICLE

Regulation of Ion Binding Sites in Covalent Organic Framework Membranes for Enhanced Selectivity under High Ionic Competition

Qing-Wei Meng,[‡] Jianguo Li,[‡] Zhiwei Xing, Weipeng Xian, Zhuozhi Lai, Zhifeng Dai, Sai Wang, Li Zhang,* Hong Yin, Shengqian Ma, and Qi Sun*

Cite This: *ACS Nano* 2025, 19, 12080−12089

Read Online

ABSTRACT: **The strategic spatial positioning of ion affinity sites within biological ion channels and their cooperative binding with the targeted ions are pivotal for enhancing ion recognition and ensuring exceptional selectivity in high ionic competition scenarios. However, the application of these principles to artificial ion channels remains largely unexplored. Herein, we present a series of covalent organic framework (COF) membranes, engineered with oxygen functional groups aligned along the rims of oriented COF pore channels of varying sizes to achieve a precise spatial arrangement of ion affinity sites. A notable COF membrane, featuring subnanometer pores decorated alternately with carbonyl and amide groups, demonstrated outstanding selectivity, achieving a Li/Mg selectivity ratio of 513 under equal mole and electrodialysis conditions. Impressively, as the Mg/Li ratio in the source solution increased to 16.6, the selectivity ratio rose to 833, significantly exceeding the reductions typically seen in conventional selective electrodialysis and nanofiltration methods. Both simulation and experimental analyses indicate that this exceptional selectivity stems from the cooperative binding between the oxygen functional groups and Li^+ ions within the confined nanochannels, facilitating the preferential transport of Li^+ ions. These findings provide a promising approach for designing selective ion extraction systems that function effectively in highly competitive environments.**

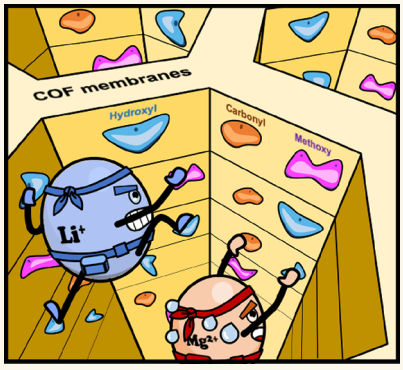

KEYWORDS: *covalent-organic-framework membranes, molecular sieving, ions channel, lithium extraction, selective separation*

INTRODUCTION

Lithium is indispensable for modern energy technologies, with its demand projected to increase 18−20 times from 2020 to 2050, primarily driven by the expanding lithium battery market.[1−5] As lithium ore reserves dwindle, the urgency to sustainably extract lithium from alternative sources, such as salt-lake brines—which account for 60−80% of the world's accessible lithium reserves—intensifies.[6−10] Efficient extraction from these sources requires effective separation of Li^+ from chemically similar ions like Mg^{2+}, which is essential for producing high-purity lithium. This separation is commonly achieved by modifying nanofiltration and selective electrodialysis membranes to carry a positive surface charge, thus enhancing their ability to repel divalent cations such as Mg^{2+} via Donnan repulsion.[11−21] However, these membranes often face challenges in maintaining their selectivity at high Mg/Li ratios. The decline in selectivity correlates with an increase in anion concentration in the permeate as the Mg^{2+} levels rise, leading to the simultaneous transport of Mg^{2+} with anions to maintain charge balance during nanofiltration, thereby reducing the efficiency of Li/Mg separation (Figure 1a).[22] In selective electrodialysis, where the migration of anions is less problematic under an electric field, a high Mg^{2+} concentration still leads to competitive adsorption issues between Mg^{2+} and Li^+.[23] The cation-exchange membranes tend to prefer the higher-charge Mg^{2+}, which occupies more ion transport sites and blocks the passage of Li^+, significantly lowering separation efficiency. Thus, producing high-purity lithium from low-grade salt-lake brines typically requires multiple stages of membrane separation, highlighting the urgent need for innovative membrane materials that improve both the selectivity and efficiency of Li^+ transport.

Received: December 15, 2024
Revised: March 10, 2025
Accepted: March 12, 2025
Published: March 18, 2025

https://doi.org/10.1021/acsnano.4c18135
ACS Nano 2025, 19, 12080−12089

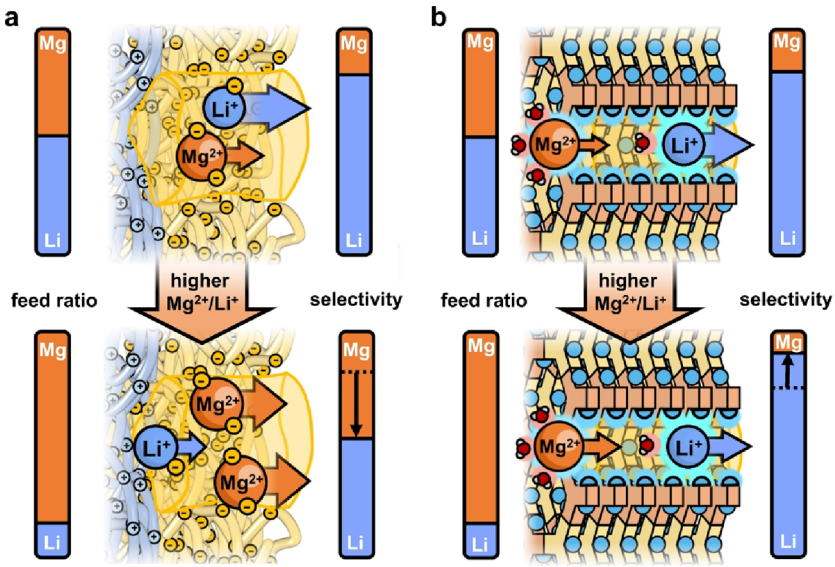

Figure 1. Comparison of membrane performance in Li^+ and Mg^{2+} separation under different ionic competition conditions. (a) Structure of cutting-edge selective electrodialysis membranes designed for Li^+ and Mg^{2+} separation under electrodialysis conditions. (b) Conceptual design of membrane materials featuring engineered affinity sites that facilitate low-barrier Li^+ ion transport, enhancing Li^+ selectivity in environments with high ionic competition.

Biological systems, refined over millions of years, display exceptional ion recognition and conductance capabilities.[22,24−27] The high efficiency of ion separation in these systems largely stems from specialized functional motifs located within their confined nanopores. For instance, the potassium ion channel KcsA demonstrates extraordinary selectivity for K^+ over Na^+ ions—with a selectivity ratio exceeding 1,000:1—thanks to strategically placed carbonyl group rings, even in environments dominated by Na^+ ions.[28] To enhance the selectivity of Li^+ over Mg^{2+} ions, particularly in conditions where Mg^{2+} predominates, it is crucial to develop membranes with affinity sites specifically engineered for low-barrier Li^+ ion transport.[29−34] While oxygen species have demonstrated substantial promise in facilitating Li^+ ion transport, optimizing the configuration of oxygen species arrays to effectively select and transport Li^+ over Mg^{2+} in environments with high Mg/Li ratios poses significant challenges. These challenges primarily stem from the complexities involved in engineering synthetic channels that mimic the precise pore structures and ion dimensions found in natural systems. Covalent organic frameworks (COFs) offer precise control over the arrangement and types of functional groups, providing a versatile platform for exploring the complex interplay between structure and function in these materials and formulating design principles for achieving high ion selectivity.[35−52]

Leveraging the versatility of COFs and the potential for lithiation of oxygen species, we tailored the distances and arrangements of oxygen-containing groups—namely carbonyl, hydroxyl, and methoxy groups—within COF membranes by pairing two monomers characterized by their distinct asymmetry and functionality. This approach resulted in COF membranes with significantly different transmembrane activation energies for Li^+ and Mg^{2+} ions. One particular COF membrane, featuring subnanometer pores patterned with alternating carbonyl and amide groups, demonstrated a Li/Mg selectivity of 513 under equal mole and electrodialysis conditions (Figure 1b). Remarkably, the selectivity ratio for Li^+ ions increased as the Mg/Li ratio in the source solution rose, reaching 833 when the initial Mg/Li ratio was 16.6—a competitiveness level comparable to that in environments like the West Taijinar brine.[53] This exceptional selectivity is attributed to cooperative binding between the oxygen species and Li^+ ions within the confined nanochannels, which effectively lower the transmembrane energy barrier and enhance the diffusion speed for Li^+ ions, while impeding the transport of Mg^{2+} ions. This research not only advances our understanding of ionic selectivity mechanisms in biological ion channels and their potential applications in nanotechnology and biotechnology but also presents a novel strategy for selectively extracting target ions in environments densely populated with competing ions.

RESULT AND DISCUSSION

Design and Fabrication of Membranes. To explore the optimal arrangement of oxygen species within COF pore channels for enhanced Li/Mg selectivity, we selected COFs with hydrazone linkages for a proof-of-concept study. These linkages are chosen for their known lithiophilicity, exceptional chemical stability, and superior geometrical and functional compatibility.[54−61] We utilized benzene-1,3,5-tricarbohydrazide (Bth) as the core building block, pairing it with triformylphloroglucinol (Tp), 2,4,6-trimethoxybenzene-1,3,5-tricarbaldehyde (Tma), 2,5-dihydroxyterephthalaldehyde (Dha), and 2,5-dimethoxyterephthalaldehyde (Dma) to synthesize four distinct COF membranes: COF-BthTp, COF-BthTma, COF-BthDha, and COF-BthDma. Each of these COFs features hexagonal prism-shaped pores with various densities and types of oxygen groups within their one-dimensional nanochannels. Preliminary computational analyses of the electrostatic potentials (ESP) within these pores revealed substantial differences in ESP distribution and intensity, indicating variations in ion-dipole interactions that could significantly affect ion selectivity (Figure 2a).

For the synthesis of these membranes, we utilized a liquid−solid−liquid interfacial polymerization technique on poly-

https://doi.org/10.1021/acsnano.4c18135
ACS Nano 2025, 19, 12080−12089

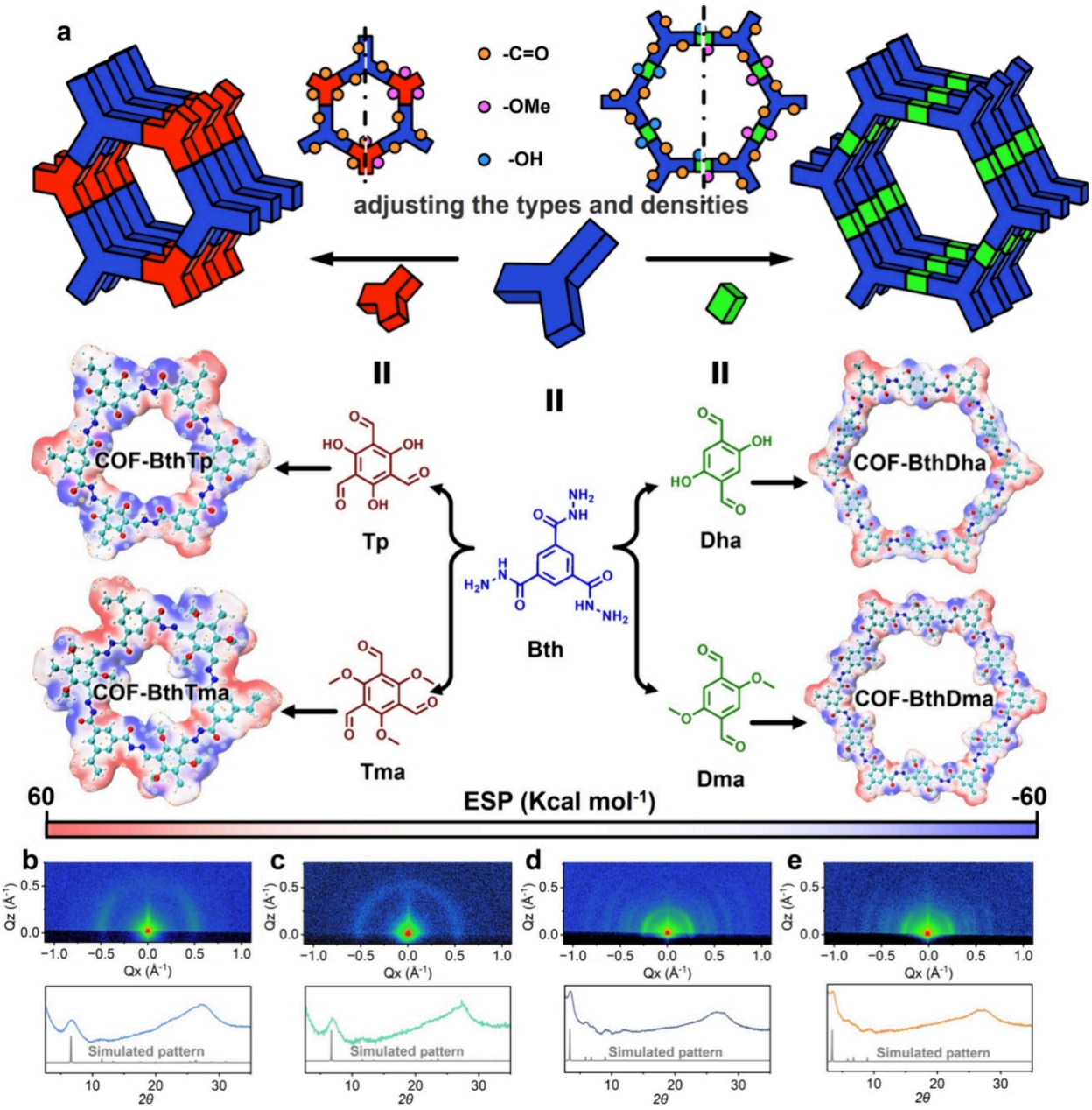

Figure 2. Membrane synthesis and characterization. (a) Depicts the chemical structures of monomers used in the synthesis of COF membranes, alongside the ESP of a hexagonal COF pore. Inset: Molecular visualization of the COFs showing C in green, O in red, N in blue, and H in white. The top portion of panels (b) COF-BthTp, (c) COF-BthTma, (d) COF-BthDha, and (e) COF-BthDma, features GIWAXS patterns, with their corresponding one-dimensional representations shown below, whereby the simulated pattern was generated using the eclipsed AA stacking structure.

acrylonitrile (PAN) ultrafiltration substrates, which have a molecular weight cutoff of 50 000 Da and feature nanoscale, relatively uniform pore sizes (20−40 nm). This uniformity is crucial for the formation of defect-free COF layers. During the synthesis process, an aqueous acetic acid solution containing Bth was applied to one side of the PAN membrane, while an organic solution containing one of the aldehydes (Tp, Tma, Dha, or Dma) was applied to the opposite side. This interfacial reaction not only resulted in visible color changes on the PAN surface, indicative of successful COF layer formation (Figure S1), but also varied the zeta potentials of the membranes, further confirming the formation (Figure S2).

Scanning electron microscopy (SEM) images of both the surface and cross-section of the membranes revealed the formation of continuous, defect-free COF layers with a thickness ranging from 114 to 128 nm (Figures S3−S7). Notably, increasing the concentration of monomers did not alter the membrane thickness, while decreasing the concentration led to the formation of defects in the membrane, as evidenced by the significantly increased ion flux (Figure S8). Fourier transform infrared (FT-IR) spectra indicated the disappearance of the N−H stretching band (3197−3298 cm^{-1}) and aldehydic C−H stretching bands (2875 and 2779 cm^{-1}), which are characteristic of the Bth and aldehyde monomers.[62] Concurrently, the emergence of the − NHCO− stretch at 1660−1680 cm^{-1} suggested the formation of hydrazone linkages within the COF membranes (Figure S9).[63] This finding was further supported by solid-state ^{13}C nuclear

https://doi.org/10.1021/acsnano.4c18135
ACS Nano 2025, 19, 12080−12089

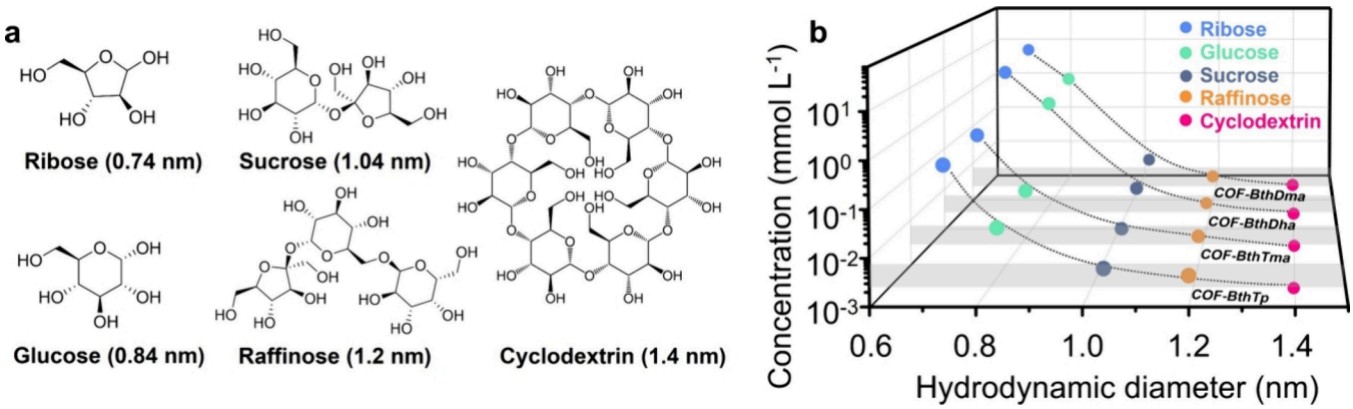

Figure 3. Assessment of membrane compactness. (a) Chemical structures and hydrodynamic diameters of various neutral organic molecules. (b) Concentration of various molecules on the permeate side across different COF membranes under dialysis conditions, with an initial concentration of 0.1 M on the feed side. The gray area indicates the detection limit for high-performance liquid chromatography (HPLC).

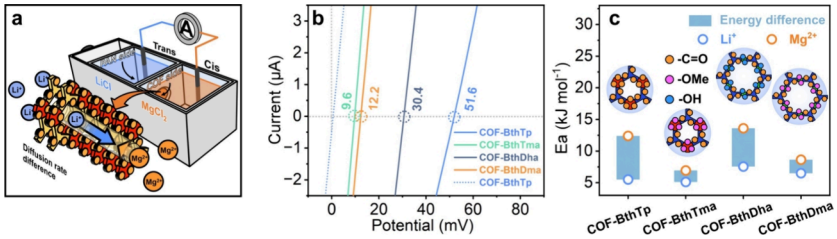

Figure 4. Investigation of transmembrane ion transport. (a) Electrochemical testing setup. (b) I−V curves collected in the presence of various COF membranes. Solid lines represent conditions with $MgCl_2$ (0.05 M) on the *cis* side and LiCl (0.1 M) on the *trans* side; dashed line represents both sides filled with $MgCl_2$ (0.05 M). (c) Comparative analysis of transmembrane activation energies for Li^+ and Mg^{2+} across various COF membranes.

magnetic resonance (NMR) spectra, which displayed a peak for the amide carbonyl carbon at 160.1−166.3 ppm, affirming the chemical structure (Figure S10).[62]

Powder X-ray diffraction (PXRD) analysis of the COF membranes, conducted after the PAN was dissolved, indicated that the COF membranes align with simulations based on the eclipsed AA stacking structure (Figures S11−S14). The pore size distributions for these COF membranes, derived from N_2 sorption isotherms, were centered at 0.79, 0.78, 1.76, and 1.58 nm for COF-BthTp, COF-BthTma, COF-BthDha, and COF-BthDma, respectively (Figures S15 and S16). Transmission electron microscopy (TEM) further confirmed the porosity and crystallinity of the membranes by revealing distinct lattice fringes that indicate one-dimensional (1D) straight porous channels, corroborating the COF structure suggested by the PXRD patterns (Figure S17). Additionally, grazing incidence wide-angle X-ray scattering (GIWAXS) provided valuable insights into the in-plane and out-of-plane structural organization of the COF membranes. The variations in scattering intensity, particularly along the vertical direction (perpendicular to the film surface, Qz = 0), highlighted the in-plane periodicity and ordering of the membrane. Projections near Qz = 0 closely matched both the calculated and experimental PXRD patterns (Figures 2b−2e), providing direct evidence of high crystallinity. Furthermore, the changes in scattering intensity along the vertical direction confirmed the oriented growth of the membranes.[64]

Before exploring the ion separation capabilities of these COF membranes, we first examined their compactness by measuring their transmembrane permeability to a series of neutral organic molecules, including ribose, glucose, sucrose, raffinose, and cyclodextrin. These molecules have hydrodynamic diameters ranging from 0.74 to 1.4 nm (Figure 3a).[65,66] The gray area in the results represents the detection limit. We found that the membranes with smaller pores—specifically COF-BthTp and COF-BthTma—effectively blocked the permeation of sucrose molecules, which have a hydrodynamic diameter of 1.04 nm. The concentration of molecules that permeated these membranes remained below the detection limits under dialysis conditions for at least 5 days. Conversely, the COF-BthDha and COF-BthDma membranes exhibited a size-exclusion cutoff at 1.2 nm in hydrodynamic diameter, further affirming their structural integrity (Figure 3b).

Investigation of Li^+ and Mg^{2+} Transmembrane Permeability. To assess the relative permeabilities of Li^+ and Mg^{2+} ions through COF membranes, we conducted reversal potential (V_r) measurements (Figure 4a). Before conducting these measurements, we ensured that the ion transmembrane transport rates were identical from both sides of the COF membrane. For this purpose, solutions of $MgCl_2$ or LiCl were introduced into the two chambers of an electrochemical cell, separated by the COF membrane. The resulting current−voltage (I−V) curves, which nearly intersected at the origin, indicative of identical ion transport rates on both sides of the membrane. To further investigate the transport rates of Li^+ and Mg^{2+} ions, 0.05 M $MgCl_2$ and 0.1 M LiCl were respectively introduced to the *cis* side (facing the COF layer) and *trans* side (against the PNA support), maintaining equal chloride ion concentrations in both chambers to focus exclusively on cation permeability. The values, determined from the x-intercepts of the I−V curves, were 51.6 mV for

https://doi.org/10.1021/acsnano.4c18135
ACS Nano 2025, 19, 12080−12089

COF-BthTp, 30.4 mV for COF-BthDha, 9.6 mV for COF-BthTma, and 12.2 mV for COF-BthDma (Figure 4b). These findings indicate a preferential transport of Li^+ over Mg^{2+}, with a decreasing trend in relative Li^+ permeability from COF-BthTp to COF-BthTma, as evidenced by the declining V_r values.

We conducted further quantitative evaluations of the transmembrane permeability differences between Li^+ and Mg^{2+} by determining their activation energies (E_a) across various COF membranes. The temperature-dependent Arrhenius behavior of ion conductivity suggested that the transport process is thermally activated. The activation energies for Li^+ transport were found to be 5.51 kJ mol^{-1} for COF-BthTp, 5.12 kJ mol^{-1} for COF-BthTma, 7.55 kJ mol^{-1} for COF-BthDha, and 6.50 kJ mol^{-1} for COF-BthDma. In contrast, Mg^{2+} exhibited activation energies of 12.41 kJ mol^{-1}, 6.94 kJ mol^{-1}, 13.60 kJ mol^{-1}, and 8.64 mol^{-1}, respectively. Notably, COF-BthTp displayed the largest differential in activation energies between Mg^{2+} and Li^+, suggesting its potential for superior selectivity (Figure 4c and Figure S18). Indeed, under single-salt conditions of 0.1 M, COF-BthTp exhibited the highest Li/Mg separation factor among the COF membranes evaluated (Figures S19 and S20). Additionally, despite its smaller pore size compared to COF-BthDha, COF-BthTp demonstrated significantly higher Li^+ permeability, more than 2 orders of magnitude greater (4.7 vs 0.039 mmol m^2 h^{-1}), emphasizing the crucial role of the type and density of oxygen species in enhancing Li^+ transport.

Investigation of Li/Mg Separation Performance. To evaluate the separation performance of membranes under conditions that mirror real operational environments, we investigated the cation transport properties of these COF membranes in a laboratory-scale electrodialysis (ED) cell (Figure S21). We tested single-salt solutions of 0.1 M LiCl and 0.1 M $MgCl_2$, as well as a binary aqueous solution containing equal concentrations of these salts. The order of Li^+ flux across different COF membranes in single-salt solutions was as follows: COF-BthTp ≈ COF-BthTma > COF-BthDma > COF-BthDha. This ranking indicates that, despite their smaller pore sizes, the COF-BthTp and COF-BthTma membranes facilitated higher Li^+ permeation rates. This can likely be attributed to the higher density of oxygen species on these membranes, which plays a more significant role in enhancing Li^+ ion transport than pore size. Specifically, the smaller pores increase the local concentration of oxygen species, thereby improving ion transport. Notably, the COF-BthTp membrane also showed the lowest Mg^{2+} flux among the tested membranes, achieving the highest single-salt ion selectivity for Li/Mg at a ratio of 209 (Figure 5a).

In binary salt ED tests, the selectivity increased significantly, demonstrating the potential of these COF membranes for Li^+ extraction. Specifically, the selectivity of the COF-BthTp membrane reached 513, while COF-BthTma, COF-BthDha, and COF-BthDma improved their selectivities from 13, 34, and 16 in single-salt conditions to 17, 178, and 24, respectively, in binary-salt conditions. These performances were benchmarked against a state-of-the-art commercial monovalent selective cation exchange membrane, CIMS (ASTOM, Japan). Here, the COF-BthTp not only recorded slightly higher monovalent ion fluxes (65 vs 58 mmol m^{-2} h^{-1}) but also demonstrated significantly enhanced selectivity (513 vs 86), underscoring its superior performance (Figure 5b). Moreover, after 10 ED cycles, no changes were observed in the XRD pattern and SEM

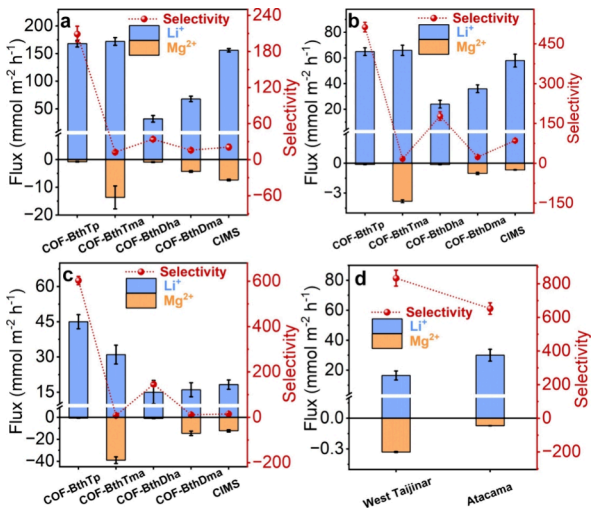

Figure 5. Comparative analysis of Li/Mg selectivity across different membranes under ED conditions. (a) Under single-salt conditions using 0.1 M LiCl and 0.1 M $MgCl_2$. (b) Under binary-salt conditions with equal concentrations of 0.1 M LiCl and 0.1 M $MgCl_2$. (c) Under binary-salt conditions with 0.1 M LiCl and 1.0 M $MgCl_2$. (d) Under binary-salt conditions utilizing artificial brine sourced from the West Taijinar (China) and Atacama (Chile) salt lakes. The ED cell operated at a consistent current density of 0.5 mA cm^{-2}. Error bars indicate standard deviations from three independent experiments.

morphology of the COF-BthTp membrane, confirming its durability during the ED process (Figures S22−S24).

It is important to note that under binary salt conditions, the COF membranes exhibited higher selectivity compared to single-salt systems, although the ion fluxes were lower. This increased selectivity can be attributed to the competitive adsorption and transport mechanisms. The membranes bind both Li^+ and Mg^{2+} ions, with a stronger affinity for Li^+. In binary solutions, this preferential binding enhances the selectivity for Li^+ over Mg^{2+}, as the competition between the ions enables the membrane to differentiate them based on their respective binding affinities. The significant decrease in flux under binary salt conditions can be explained by two main factors: (1) The presence of divalent Mg^{2+} ions, combined with the higher overall ion concentration in the mixed salt system, results in a substantially higher osmotic pressure compared to single-salt conditions. This increased osmotic pressure reduces the effective driving force for ion transport, thereby lowering the flux. (2) Multivalent ions such as Mg^{2+} diffuse more slowly than monovalent ions, causing them to accumulate on the membrane surface. This accumulation creates a high-concentration boundary layer, which exacerbates concentration polarization. The resulting increase in osmotic pressure near the membrane surface further reduces the flux. The observed reduction in flux in binary solutions, relative to single-salt conditions, is consistent with findings from other membrane separation systems.[39,47]

In the context of salt-lake environments, where Mg^{2+} concentrations substantially exceed those of Li^+, we assessed the selectivity of various membranes with Mg^{2+} concentrations 10-fold higher than Li^+ (1 M vs 0.1 M) under ED conditions. Remarkably the COF-BthTp membrane exhibited enhanced selectivity in these high Mg^{2+}-to-Li^+ conditions, increasing from a selectivity value of 513 (under equimolar conditions of 0.1 M each) to 603. Conversely, other membranes, including

https://doi.org/10.1021/acsnano.4c18135
ACS Nano 2025, 19, 12080−12089

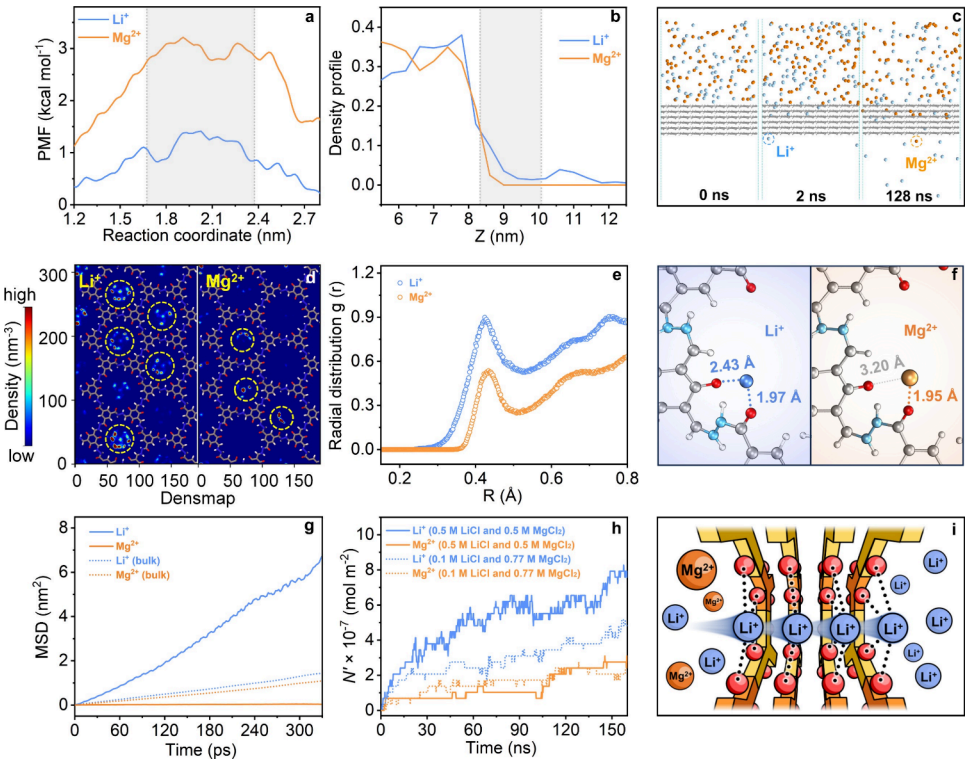

Figure 6. Detailed molecular-level analysis of high Li^+ conductance across the COF-BthTp membrane. (a) PMF profiles for Li^+ and Mg^{2+} ions across the COF-BthTp membrane, with gray dashed lines marking the membrane boundaries. (b) Ion density profiles along the *z*-axis within the COF, with gray dashed lines marking the membrane boundaries. (c) Simulation snapshots showing the transmembrane transport of Li^+ and Mg^{2+} ions (colored bule and orange, respectively). (d) A 2D density map illustrating the distribution of Li^+ and Mg^{2+} ions across the *xy* plane of the membrane. (e) RDF between the ions and the oxygen atoms on the COF-BthTp membrane. (f) Binding interactions between Li^+, Mg^{2+}, and the COF-BthTp structure. (g) Comparison of the diffusion coefficients of Li^+ and Mg^{2+} ions across the COF-BthTp membrane and in bulk solution, with emphasis on mean square displacement (MSD). (h) Transmembrane ion permeation kinetics characterized by MD simulations under binary conditions. (i) Schematic representation of ion partitioning, conduction, and the enhanced selectivity of Li^+ over Mg^{2+} across the COF-BthTp membrane.

COF-BthTma, COF-BthDha, COF-BthDma, and the commercial ASTOM membrane, showed significant decreases in selectivity, with values declining from 17, 178, 24, and 86 to 8, 146, 11, and 15, respectively (Figure 5c). Furthermore, the COF-BthTp membrane demonstrated long-term stability under high Mg^{2+} concentration conditions, maintaining consistent performance in both ion flux and selectivity over at least 10 cycles (Figure S25).

In light of the superior separation performance of the COF-BthTp membrane, we broadened our study to examine its ability to separate Li^+ and Mg^{2+} using synthetic salt-lake brines designed to emulate the ion concentrations typical of natural salt lakes. We prepared artificial brines mimicking those from the Atacama (Chile) and West Taijinar (China) salt lakes, with initial Mg^{2+}-to-Li^+ mole ratios of 1.6 (0.72 mol L^{-1} Mg^{2+} vs 0.44 mol L^{-1} Li^+) and 16.6 (0.63 mol L^{-1} Mg^{2+} vs 0.038 mol L^{-1} Li^+), respectively (Table S1). Utilizing the COF-BthTp membrane under ED conditions, the Mg^{2+} to Li^+ mole ratios significantly decreased from 1.6 and 16.6 to 0.0024 and 0.02, respectively. These results translate to Li/Mg mole selectivities of 653 and 833, indicating a notable increase in selectivity at higher initial Mg^{2+} to Li^+ ratios, thus underscoring the potential of COF-BthTp for efficient Li^+ extraction from low-grade brines (Figure 5d and Table S2).

Molecular Dynamics (MD) Simulations. To explore the superior ion-screening properties of the COF-BthTp membrane, MD simulations were conducted to assess the transport behaviors of Li^+ and Mg^{2+} ions. These simulations utilized binary systems with 0.5 M solutions of LiCl and $MgCl_2$. The potential of mean force (PMF) profiles was first calculated to capture the energy changes as ions approach, traverse, and exit the COF membrane. To reduce computational cost while maintaining essential energy trends, a simplified three-layer COF membrane was used for the PMF profile calculations. The PMF profiles exhibited a gradual increase in energy as both Mg^{2+} and Li^+ ions approached the membrane pores, followed by a plateau as they passed through the membrane, and a decrease after exiting. This indicated that Mg^{2+} ions encountered higher energy barriers during transmembrane migration compared to Li^+ ions (Figure 6a). Encouraged by these results, a six-layer COF membrane was employed to enhance the role of membrane in the MD simulation (Figure S26). Number density distributions along the *z*-axis revealed a significant accumulation of Li^+ ions within and on the permeate side of the membrane, indicating a more rapid translocation of Li^+ ions (Figure 6b). Ion trajectory analysis confirmed faster transmembrane transport rates for Li^+ over Mg^{2+} (Figure 6c). Spatial distribution analysis in the xy plane within the pore channels revealed clustering of Li^+ ions at the edges of the COF channels, in contrast to the sparser distribution of Mg^{2+} ions (Figure 6d). Radial distribution function (RDF) analysis between the oxygen atoms in the COF and the ions showed a higher peak for Li^+ compared to Mg^{2+}, indicating that Li^+ ions are more likely to occupy well-

https://doi.org/10.1021/acsnano.4c18135
ACS Nano 2025, 19, 12080−12089

defined coordination sites near the oxygen atoms (Figure 6e). Additionally, density functional theory (DFT) calculations confirmed that two adjacent oxygen atoms in COF-BthTp could cooperatively bind to Li^+ ions, unlike the interactions with Mg^{2+} ions, which predominantly involved oxygen atoms from hydrazone linkages (Figure 6f). This disparity in interaction led to a distinct preference for Li^+ ion passage through the COF-BthTp channels. This is supported by significantly higher transmembrane diffusion coefficients for Li^+ (4.0×10^{-5} cm^2 s^{-1}) compared to Mg^{2+} (2.5×10^{-7} cm^2 s^{-1}). In the solution, the diffusion coefficients were 1.0×10^{-5} cm^2 s^{-1} for Li^+ and 0.7×10^{-5} cm^2 s^{-1} for Mg^{2+}, indicating that the COF-BthTp channels specifically enhance Li^+ transport while impeding Mg^{2+} movement (Figure 6g). Additionally, monitoring the normalized number of permeated ions (N') over time consistently showed higher values for N'_{Li} compared to N'_{Mg}, with Li/Mg selectivity ratios around 2.9. When the Mg/Li ratio in the feed solution increased to 0.77 M $MgCl_2$ and 0.1 M LiCl, MD simulations continued to show a preference for Li^+ ion transport, even in the presence of a high Mg^{2+} concentration.

After considering the initial concentrations of Li^+ and Mg^{2+}, the Li/Mg selectivity ratio increased to 3.9, indicating enhanced Li^+ selectivity at higher Mg/Li ratios, which aligns with our experimental findings (Figure 6h). These findings suggest that Li^+ ions are more readily coordinated with the oxygen species and once coordinated with the membrane binding sites, are driven toward the next relay moiety—subsequent COF layers—by the ion gradient across the membrane. The eclipsed AA stacking structure of COF-BthTp facilitates efficient site-to-site hopping, similar to the knock-on mechanisms observed in biological ion channels (Figure 6i).[24,28] This mechanism explains the enhanced selectivity at higher Mg^{2+}/Li^+ ratios. Although the absolute flux of Mg^{2+} may increase with its higher concentration, the relative increase in Mg^{2+} transport is smaller compared to the increase in its concentration. This discrepancy further amplifies the Li^+/Mg^{2+} selectivity.

CONCLUSION

In summary, we have successfully synthesized a series of COF membranes with oriented pore structures, strategically positioning various oxygen species along the channel walls to modulate the transmembrane activation energy for Li^+ and Mg^{2+} ions. The optimized COF membrane, featuring alternating amide and carbonyl oxygen groups within subnanoscale pore channels, exhibited exceptional Li/Mg selectivity and permeability. This design significantly outperformed leading commercial membranes in lithium recovery, achieving a selectivity more than 40fold greater, particularly under conditions with a high Mg/Li ratio. Theoretical calculations suggest that the cooperative binding between adjacent amide and carbonyl oxygen groups, aligned within the oriented eclipsed AA stacking pore structure, plays a critical role in facilitating site-to-site hopping along the pore channel. This feature is crucial for enhancing Li^+ over Mg^{2+} selectivity under competitive conditions. Such a characteristic is especially advantageous for extracting lithium from low-grade salt-lake brines, offering a highly effective solution in challenging extraction environments. Overall, this study establishes foundational design principles for ion-separating membranes and proves invaluable for selective ion extraction in competitive scenarios.

EXPERIMENTAL SECTION

Fabrication of the COF Membranes. *COF-BthTp.* The COF membrane was synthesized through interfacial polymerization on the surface of a PAN ultrafiltration membrane, which has a molecular weight cutoff of 50 000 Da. The PAN support was positioned vertically in the center of a custom-built diffusion cell, each chamber holding a volume of 7 cm^3. An aqueous solution containing Bth (18 mg, 0.07 mmol) in 3 M acetic acid (7 mL) was introduced on one side of the diffusion cell, while the organic phase containing Tp (15 mg, 0.07 mmol) in a mixture of ethyl acetate and mesitylene (V/V = 1/5, 7 mL) was introduced on the opposite side. The reaction was allowed to proceed at 35 °C for 6 days. After completion, the membrane was sequentially washed with ethanol, methanol, and water to eliminate any residual monomers, catalysts, and organic solvents before it was subjected to performance testing.

COF-BthTma. The COF-BthTma membrane was synthesized following the same procedure used for the COF-BthTp membrane, except that Tma (17.7 mg, 0.07 mmol) dissolved in a mixture of ethyl acetate and mesitylene (V/V = 1/5, 7 mL) was used as the organic phase.

COF-BthDha. The COF-BthTma membrane was synthesized following the same precudure used for the COF-BthTp membrane, except that Dha (17.8 mg, 0.11 mmol) dissolved in a mixture of ethyl acetate and mesitylene (V/V = 1/5, 7 mL) was used as the organic phase.

COF-BthDma. The COF-BthDma membrane was synthesized following the same precudure used for the COF-BthTp membrane, except that Dma (21.4 mg, 0.11 mmol) dissolved in the mixture of ethyl acetate and mesitylene (V/V = 1/5, 7 mL) was used as the organic phase.

Ion Separation Performance Evaluation. Selective electrodialysis tests were performed at a current density of 0.5 mA cm^{-2} using the setup shown as below (Figure S21). The COF active layer was set to face the anode. A 400 mL solution of 0.3 M Na_2SO_4 was used to circulate in the electrodes compartments. The feed side contained 400 mL of 0.1 M LiCl/$MgCl_2$ solution and the permeate side was filled with 400 mL of 0.01 M KCl solution. All solutions were circulated by peristaltic pumps at a flow rate of 80 mL min^{-1}. The concentrations of Li^+ and Mg^{2+} in the permeate side were analyzed by ion chromatography.

ASSOCIATED CONTENT

Supporting Information

The Supporting Information is available free of charge at https://pubs.acs.org/doi/10.1021/acsnano.4c18135.

Materials and characterization, dialysis experiments, neutral organic molecule permeability experiments, transmembrane activation energy measurement, electrostatic potential simulation, binding energy calculation, molecular dynamics simulations; characterizations including zeta potentials, SEM, FT-IR spectra, solid-state ^{13}C NMR spectra, BET, TEM, apparent activation energy, evaluation of membrane performance and recyclability, and simulation schematic representation; ion concentrations in the brines and comparison of the Li/Mg separation performances (PDF)

AUTHOR INFORMATION

Corresponding Authors

Li Zhang − *Key Laboratory of Surface & Interface Science of Polymer Materials of Zhejiang Province, School of Chemistry and Chemical Engineering, Zhejiang Sci-Tech University, Hangzhou 310018, China*; Email: lizhang@zstu.edu.cn

Qi Sun − *Zhejiang Provincial Key Laboratory of Advanced Chemical Engineering Manufacture Technology, College of Chemical and Biological Engineering, Zhejiang University,*

https://doi.org/10.1021/acsnano.4c18135
ACS Nano 2025, 19, 12080−12089

Hangzhou 310027, China; orcid.org/0000-0002-1698-8741; Email: sunqichs@zju.edu.cn

Authors

Qing-Wei Meng − *Zhejiang Provincial Key Laboratory of Advanced Chemical Engineering Manufacture Technology, College of Chemical and Biological Engineering, Zhejiang University, Hangzhou 310027, China;* orcid.org/0009-0005-5967-4848

Jianguo Li − *Key Laboratory of Surface & Interface Science of Polymer Materials of Zhejiang Province, School of Chemistry and Chemical Engineering, Zhejiang Sci-Tech University, Hangzhou 310018, China*

Zhiwei Xing − *Zhejiang Provincial Key Laboratory of Advanced Chemical Engineering Manufacture Technology, College of Chemical and Biological Engineering, Zhejiang University, Hangzhou 310027, China*

Weipeng Xian − *Zhejiang Provincial Key Laboratory of Advanced Chemical Engineering Manufacture Technology, College of Chemical and Biological Engineering, Zhejiang University, Hangzhou 310027, China*

Zhuozhi Lai − *Zhejiang Provincial Key Laboratory of Advanced Chemical Engineering Manufacture Technology, College of Chemical and Biological Engineering, Zhejiang University, Hangzhou 310027, China*

Zhifeng Dai − *Key Laboratory of Surface & Interface Science of Polymer Materials of Zhejiang Province, School of Chemistry and Chemical Engineering, Zhejiang Sci-Tech University, Hangzhou 310018, China; Longgang Institute of Zhejiang Sci-Tech University, Wenzhou 325802, China*

Sai Wang − *Hangzhou Institute of Advanced Studies, Zhejiang Normal University, Hangzhou 310015, China*

Hong Yin − *Zhejiang Provincial Key Laboratory of Advanced Chemical Engineering Manufacture Technology, College of Chemical and Biological Engineering, Zhejiang University, Hangzhou 310027, China;* orcid.org/0000-0003-0742-3754

Shengqian Ma − *Department of Chemistry, University of North Texas, Denton, Texas 76201, United States;* orcid.org/0000-0002-1897-7069

Complete contact information is available at: https://pubs.acs.org/10.1021/acsnano.4c18135

Author Contributions

‡Q.-W.M. and J.L. contributed equally.

Notes

The authors declare no competing financial interest.

ACKNOWLEDGMENTS

This work was supported by the National Key Research and Development Program of China (2024YFB3815700), the National Science Foundation of China (22421004), and the National Science Foundation of Zhejiang province (LR23B060001).

REFERENCES

(1) Zhang, G.; Li, Y.; Guan, X.; Hu, G.; Su, H.; Xu, X.; Feng, G.; Shuchi, S. B.; Kim, S. C.; Zhou, J.; Xu, R.; Xiao, X.; Wu, A.; Cui, Y. Spontaneous lithium extraction and enrichment from brine with net energy output driven by counter-ion gradients. *Nat. Water* **2024**, *2*, 1091−1101.

(2) Peng, Q.; Wang, R.; Zhao, Z.; Lin, S.; Liu, Y.; Dong, D.; Wang, Z.; He, Y.; Zhu, Y.; Jin, J.; Jiang, L. Extreme Li-Mg selectivity via precise ion size differentiation of polyamide membrane. *Nat. Commun.* **2024**, *15*, 2505.

(3) Xue, N.; Wu, X.; Shi, H.; Zhang, Y.; Zhang, Y.; Lv, Y.; Zhang, X.; Chen, X.; Yu, Y.; Liu, W. Single lithium-ion conductor decorated $LiMn_2O_4$ with high selectivity and stability for electrochemical lithium extraction. *ACS Nano* **2024**, *18*, 33743−33753.

(4) Lv, Y.; Dai, Z.; Chen, Y.; Lu, Y.; Zhang, X.; Yu, J.; Zhai, W.; Yu, Y.; Wen, Z.; Cui, Y.; Liu, W. Two-dimensional sulfonate-functionalized metal-organic framework membranes for efficient lithium-ion sieving. *Nano Lett.* **2024**, *24*, 2782−2788.

(5) Lv, Y.; Dong, L.; Cheng, L.; Gao, T.; Wu, C.; Chen, X.; He, T.; Cui, Y.; Liu, W. Tailoring monovalent ion sieving in graphene-oxide membranes with high flux by rationally intercalating crown ethers. *ACS Appl. Mater. Interfaces* **2023**, *15*, 46261−46268.

(6) Yan, G.; Wang, M.; Hill, G. T.; Zou, S.; Liu, C. Defining the challenges of Li extraction with olivine host: The roles of competitor and spectator ions. *Proc. Natl. Acad. Sci. U. S. A.* **2022**, *119*, No. e2200751119.

(7) Song, Y.; Fang, S.; Xu, N.; Wang, M.; Chen, S.; Chen, J.; Mi, B.; Zhu, J. Solar transpiration-powered lithium extraction and storage. *Science* **2024**, *385*, 1444−1449.

(8) Xia, Q.; Deng, Z.; Sun, S.; Zhao, W.; Ding, J.; Xi, B.; Gao, G.; Wang, C. Solar-enhanced lithium extraction with self-sustaining water recycling from salt-lake brines. *Proc. Natl. Acad. Sci. U. S. A.* **2024**, *121*, No. e2400159121.

(9) Li, Z.; Chen, I.-C.; Cao, L.; Liu, X.; Huang, K.-W.; Lai, Z. Lithium extraction from brine through a decoupled and membrane-free electrochemical cell design. *Science* **2024**, *385*, 1438−1444.

(10) Zhang, Y.; Zhou, K.; Su, S.; Gao, J.; Liu, J.; Jiang, L. Congener-welded crystalline carbon nitride membrane for robust and highly selective Li/Mg separation. *Sci. Adv.* **2024**, *10*, No. eadm9620.

(11) Yuan, B.; Zhang, Y.; Qi, P.; Yang, D.; Hu, P.; Zhao, S.; Zhang, K.; Zhang, X.; You, M.; Cui, J.; Jiang, J.; Lou, X.; Niu, Q. J. Self-assembled dendrimer polyamide nanofilms with enhanced effective pore area for ion separation. *Nat. Commun.* **2024**, *15*, 471.

(12) Wang, R.; He, R.; He, T.; Elimelech, M.; Lin, S. Performance metrics for nanofiltration-based selective separation for resource extraction and recovery. *Nat. Water* **2023**, *1*, 291−300.

(13) Guo, B. B.; Liu, C.; Zhu, C. Y.; Xin, J. H.; Zhang, C.; Yang, H. C.; Xu, Z. K. Double charge flips of polyamide membrane by ionic liquid-decoupled bulk and interfacial diffusion for on-demand nanofiltration. *Nat. Commun.* **2024**, *15*, 2282.

(14) Zhao, S.; Zhao, Z.; Zhang, X.; Zha, Z.; Tong, T.; Wang, R.; Wang, Z. Polyamide membranes with tunable surface charge induced by dipole-dipole interaction for selective ion separation. *Environ. Sci. Technol.* **2024**, *58*, 5174−5185.

(15) Liu, M.-L.; Zhang, C.-X.; Tang, M.-J.; Sun, S.-P.; Xing, W.; Lee, Y. M. Evolution of functional nanochannel membranes. *Prog. Mater. Sci.* **2023**, *139*, No. 101162.

(16) Peng, H.; Zhang, W.; Hung, W.; Wang, N.; Sun, J.; Lee, K.; An, Q.; Liu, C.; Zhao, Q. Phosphonium modification leads to ultra-permeable antibacterial polyamide composite membranes with unreduced thickness. *Adv. Mater.* **2020**, *32*, 2001383.

(17) Zhang, M.; Guan, K.; Ji, Y.; Liu, G.; Jin, W.; Xu, N. Controllable ion transport by surface-charged graphene oxide membrane. *Nat. Commun.* **2019**, *10*, 1253.

(18) Lu, Z.; Wu, Y.; Ding, L.; Wei, Y.; Wang, H. A lamellar MXene ($Ti_3C_2T_x$)/PSS composite membrane for fast and selective lithium-ion separation. *Angew. Chem., Int. Ed.* **2021**, *60*, 22265−22269.

(19) Xu, S.; Lin, H.; Li, G.; Han, Q.; Wang, J.; Liu, F. Heterogeneous covalent organic framework membranes mediated by polycations for efficient ions separation. *Adv. Sci.* **2024**, *11*, 2405539.

(20) Lin, J.; Ye, W.; Xie, S.; Du, J.; Liu, R.; Zou, D.; Chen, X.; Yu, Z.; Fang, S.; Ang, E. Y. M.; Toh, W.; Han, D. D.; Ng, T. Y.; Seo, D. H.; Zhao, S.; Van der Bruggen, B.; Xie, M.; Lee, Y. M. Shielding effect enables fast ion transfer through nanoporous membrane for highly energy-efficient electrodialysis. *Nat. Water* **2023**, *1*, 725−735.

(21) Razmjou, A.; Asadnia, M.; Hosseini, E.; Habibnejad Korayem, A.; Chen, V. Design principles of ion selective nanostructured membranes for the extraction of lithium ions. *Nat. Commun.* **2019**, *10*, 5793.
(22) Hong, S.; Di Vincenzo, M.; Tiraferri, A.; Bertozzi, E.; Górecki, R.; Davaasuren, B.; Li, X.; Nunes, S. P. Precision ion separation via self-assembled channels. *Nat. Commun.* **2024**, *15*, 3160.
(23) Chen, Q.-B.; Ji, Z.-Y.; Liu, J.; Zhao, Y.-Y.; Wang, S.-Z.; Yuan, J.-S. Development of recovering lithium from brines by selective-electrodialysis: Effect of coexisting cations on the migration of lithium. *J. Membr. Sci.* **2018**, *548*, 408−420.
(24) Doyle, D. A.; Cabral, J. M.; Pfuetzner, R. A.; Kuo, A.; Gulbis, J. M.; Cohen, S. L.; Chait, B. T.; MacKinnon, R. The structure of the potassium channel: Molecular basis of K^+ conduction and selectivity. *Science* **1998**, *280*, 69−77.
(25) Yang, Y.; Yang, X.; Liang, L.; Gao, Y.; Cheng, H.; Li, X.; Zou, M.; Ma, R.; Yuan, Q.; Duan, X. Large-area graphene-nanomesh/carbon-nanotube hybrid membranes for ionic and molecular nanofiltration. *Science* **2019**, *364*, 1057−1062.
(26) Wang, J.; Zhang, X.; Shen, R.; Yuan, Q.; Yang, Y. Staggered-stacking two-dimensional covalent organic framework membranes for molecular and ionic sieving. *ACS Nano* **2024**, *18*, 34698−34707.
(27) Zhang, Y.; Chen, D.; He, W.; Tan, J.; Yang, Y.; Yuan, Q. Bioinspired solid-state ion nanochannels: insight from channel fabrication and ion transport. *Adv. Mater. Technol.* **2023**, *8*, 2202014.
(28) Morizumi, T.; Kim, K.; Li, H.; Govorunova, E. G.; Sineshchekov, O. A.; Wang, Y.; Zheng, L.; Bertalan, É.; Bondar, A. N.; Askari, A.; Brown, L. S.; Spudich, J. L.; Ernst, O. P. Structures of channelrhodopsin paralogs in peptidiscs explain their contrasting K^+ and Na^+ selectivities. *Nat. Commun.* **2023**, *14*, 4365.
(29) Yong, M.; Tang, M.; Sun, L.; Xiong, F.; Xie, L.; Zeng, G.; Ren, X.; Wang, K.; Cheng, Y.; Li, Z.; Li, E.; Zhang, X.; Wang, H. Sustainable lithium extraction and magnesium hydroxide co-production from salt-lake brines. *Nat. Sustain.* **2024**, *7*, 1662−1671.
(30) Violet, C.; Ball, A.; Heiranian, M.; Villalobos, L. F.; Zhang, J.; Uralcan, B.; Kulik, H.; Haji-Akbari, A.; Elimelech, M. Designing membranes with specific binding sites for selective ion separations. *Nat. Water* **2024**, *2*, 706−718.
(31) Guo, Z.; Zhang, Y.; Dong, Y.; Li, J.; Li, S.; Shao, P.; Feng, X.; Wang, B. Fast ion transport pathway provided by polyethylene glycol confined in covalent organic frameworks. *J. Am. Chem. Soc.* **2019**, *141*, 1923−1927.
(32) Chen, Z.; Hu, C.; Lu, C.; Sun, J.; Zhang, Y.; Wang, F.; Qu, J. Steric hindrance-induced dehydration promotes cation selectivity in trans-subnanochannel transport. *ACS Nano* **2023**, *17*, 12629−12640.
(33) Xu, T.; Wu, B.; Li, W.; Li, Y.; Zhu, Y.; Sheng, F.; Li, Q.; Ge, L.; Li, X.; Wang, H.; Xu, T. Perfect confinement of crown ethers in MOF membrane for complete dehydration and fast transport of monovalent ions. *Sci. Adv.* **2024**, *10*, No. eadn0944.
(34) Xin, W.; Fu, J.; Qian, Y.; Fu, L.; Kong, X. Y.; Ben, T.; Jiang, L.; Wen, L. Biomimetic KcsA channels with ultra-selective K^+ transport for monovalent ion sieving. *Nat. Commun.* **2022**, *13*, 1701.
(35) Liu, X.; Wang, J.; Shang, Y.; Yavuz, C. T.; Khashab, N. M. Ionic covalent organic framework-based membranes for selective and highly permeable molecular sieving. *J. Am. Chem. Soc.* **2024**, *146*, 2313−2318.
(36) Peng, H. Y.; Lau, S. K.; Yong, W. F. Recent advances of thin film composite nanofiltration membranes for Mg^{2+}/Li^+ separation. *Adv. Membr.* **2024**, *4*, No. 100093.
(37) Liu, Q.; Liu, M.; Zhang, Z.; Yin, C.; Long, J.; Wei, M.; Wang, Y. Covalent organic framework membranes with vertically aligned nanorods for efficient separation of rare metal ions. *Nat. Commun.* **2024**, *15*, 9221.
(38) Wang, W.; Zhang, Y.; Wang, C.; Sun, H.; Guo, J.; Shao, L. Simultaneous manipulation of membrane enthalpy and entropy barriers towards superior ion separations. *Angew. Chem., Int. Ed.* **2024**, *63*, No. e202408963.
(39) Meng, Q. W.; Zhu, X.; Xian, W.; Wang, S.; Zhang, Z.; Zheng, L.; Dai, Z.; Yin, H.; Ma, S.; Sun, Q. Enhancing ion selectivity by tuning solvation abilities of covalent-organic-framework membranes. *Proc. Natl. Acad. Sci. U. S. A.* **2024**, *121*, No. e2316716121.
(40) Kong, Y.; Lyu, B.; Fan, C.; Yang, Y.; Wang, X.; Shi, B.; Jiang, J.; Wu, H.; Jiang, Z. Manipulation of cationic group density in covalent organic framework membranes for efficient anion transport. *J. Am. Chem. Soc.* **2023**, *145*, 27984−27992.
(41) Liu, J.; Wang, S.; Huang, T.; Manchanda, P.; Abou-Hamad, E.; Nunes, S. P. Smart covalent organic networks (CONs) with "on-off-on" light-switchable pores for molecular separation. *Sci. Adv.* **2020**, *6*, No. eabb3188.
(42) Wang, K.; Yang, H.; Liao, Z.; Li, S.; Hambsch, M.; Fu, G.; Mannsfeld, S. C. B.; Sun, Q.; Zhang, T. Monolayer-assisted surface-initiated Schiff-base-mediated aldol polycondensation for the synthesis of crystalline sp^2 carbon-conjugated covalent organic framework thin films. *J. Am. Chem. Soc.* **2023**, *145*, 5203−521.
(43) Zhou, L.; Li, X.; Cao, K.; Jia, Z.; Long, H.; Li, Y.; Tao, G.; Liu, N.; Zhang, J.; Ma, L. Covalent organic framework membrane with turing structures for deacidification of highly acidic solutions. *Adv. Funct. Mater.* **2022**, *32*, 2108178.
(44) Xu, F.; Dai, L.; Wu, Y.; Xu, Z. Li^+/Mg^{2+} separation by membrane separation: The role of the compensatory effect. *J. Membr. Sci.* **2021**, *636*, No. 119542.
(45) Wu, C.; Xia, L.; Xia, S.; Van der Bruggen, B.; Zhao, Y. Advanced covalent organic framework-based membranes for recovery of ionic resources. *Small* **2023**, *19*, 2206041.
(46) Cao, L.; Chen, I. C.; Li, Z.; Liu, X.; Mubashir, M.; Nuaimi, R. A.; Lai, Z. Switchable Na^+ and K^+ selectivity in an amino acid functionalized 2D covalent organic framework membrane. *Nat. Commun.* **2022**, *13*, 7894.
(47) Sheng, F.; Wu, B.; Li, X.; Xu, T.; Shehzad, M. A.; Wang, X.; Ge, L.; Wang, H.; Xu, T. Efficient ion sieving in covalent organic framework membranes with sub-2-nanometer channels. *Adv. Mater.* **2021**, *33*, 2104404.
(48) Pan, Y.; Liu, H.; Huang, Z.; Zhang, W.; Gao, H.; Liang, L.; Dong, L.; Meng, H. Membranes based on covalent organic frameworks through green and scalable interfacial polymerization using ionic liquids for antibiotic desalination. *Angew. Chem., Int. Ed.* **2024**, *63*, No. e202316315.
(49) Yang, J.; Tu, B.; Zhang, G.; Liu, P.; Hu, K.; Wang, J.; Yan, Z.; Huang, Z.; Fang, M.; Hou, J.; Fang, Q.; Qiu, X.; Li, L.; Tang, Z. Advancing osmotic power generation by covalent organic framework monolayer. *Nat. Nanotechnol.* **2022**, *17*, 622−628.
(50) Yang, H.; Xu, J.; Cao, H.; Wu, J.; Zhao, D. Recovery of homogeneous photocatalysts by covalent organic framework membranes. *Nat. Commun.* **2023**, *14*, 2726.
(51) Burke, D. W.; Jiang, Z.; Livingston, A. G.; Dichtel, W. R. 2D covalent organic framework membranes for liquid-phase molecular separations: State of the field, common pitfalls, and future opportunities. *Adv. Mater.* **2024**, *36*, 2300525.
(52) Liu, L.; Yin, L.; Cheng, D.; Zhao, S.; Zang, H.-Y.; Zhang, N.; Zhu, G. Surface-mediated construction of an ultrathin free-standing covalent organic framework membrane for efficient proton conduction. *Angew. Chem., Int. Ed.* **2021**, *60*, 14875−14880.
(53) Wu, L.; Zhang, C.; Kim, S.; Hatton, T. A.; Mo, H.; Waite, T. D. Lithium recovery using electrochemical technologies: Advances and challenges. *Water Res.* **2022**, *221*, No. 118822.
(54) Li, Y.; Sui, J.; Cui, L.-S.; Jiang, H.-L. Hydrogen bonding regulated flexibility and disorder in hydrazone-linked covalent organic frameworks. *J. Am. Chem. Soc.* **2023**, *145*, 1359−1366.
(55) Liu, R.; Chen, Y.; Yu, H.; Položij, M.; Guo, Y.; Sum, T. C.; Heine, T.; Jiang, D. Linkage-engineered donor-acceptor covalent organic frameworks for optimal photosynthesis of hydrogen peroxide from water and air. *Nat. Catal.* **2024**, *7*, 195−206.
(56) Li, X. T.; Li, M. J.; Tian, Y. L.; Han, S. L.; Cai, L.; Ma, H. C.; Zhao, Y. Q.; Chen, G. J.; Dong, Y. B. A reversible photochromic covalent organic framework. *Nat. Commun.* **2024**, *15*, 8484.
(57) Liu, T.; Zhang, Y.; Shan, Z.; Wu, M.; Li, B.; Sun, H.; Su, G.; Wang, R.; Zhang, G. Covalent organic framework membrane for

efficient removal of emerging trace organic contaminants from water. *Nat. Water* **2023**, *1*, 1059−1067.
(58) Zhang, G.; Hong, Y.; Nishiyama, Y.; Bai, S.; Kitagawa, S.; Horike, S. Accumulation of glassy poly(ethylene oxide) anchored in a covalent organic framework as a solid-state Li^+ electrolyte. *J. Am. Chem. Soc.* **2019**, *141*, 1227−1234.
(59) Guo, X.; Mao, T.; Wang, Z.; Cheng, P.; Chen, Y.; Ma, S.; Zhang, Z. Fabrication of photoresponsive crystalline artificial muscles based on PEGylated covalent organic framework membranes. *ACS Cent. Sci.* **2020**, *6*, 787−794.
(60) Li, X.; Xu, H.-S.; Leng, K.; Chee, S. W.; Zhao, X.; Jain, N.; Xu, H.; Qiao, J.; Gao, Q.; Park, I.-H.; Quek, S. Y.; Mirsaidov, U.; Loh, K. P. Partitioning the interlayer space of covalent organic frameworks by embedding pseudorotaxanes in their backbones. *Nat. Chem.* **2020**, *12*, 1115−1122.
(61) Karak, S.; Singh, H.; Biswas, A.; Paul, S.; Manna, S.; Nishiyama, Y.; Pathak, B.; Banerjee, A.; Banerjee, R. Lithiophilic dibenzamide linkages to impart lithium storage capacity in porous polybenzamides. *J. Am. Chem. Soc.* **2024**, *146*, 20183−20192.
(62) Yin, S.; Li, J.; Lai, Z.; Meng, Q. W.; Xian, W.; Dai, Z.; Wang, S.; Zhang, L.; Xiong, Y.; Ma, S.; Sun, Q. Giant gateable thermoelectric conversion by tuning the ion linkage interactions in covalent organic framework membranes. *Nat. Commun.* **2024**, *15*, 8137.
(63) Tang, J.; Liang, Z.; Qin, H.; Liu, X.; Zhai, B.; Su, Z.; Liu, Q.; Lei, H.; Liu, K.; Zhao, C.; Cao, R.; Fang, Y. Large-area free-standing metalloporphyrin-based covalent organic framework films by liquid-air interfacial polymerization for oxygen electrocatalysis. *Angew. Chem., Int. Ed.* **2023**, *62*, No. e202214449.
(64) Wang, Z.; Walter, L. S.; Wang, M.; Petkov, P. S.; Liang, B.; Qi, H.; Nguyen, N. N.; Hambsch, M.; Zhong, H.; Wang, M.; Park, S.; Renn, L.; Watanabe, K.; Taniguchi, T.; Mannsfeld, S. C. B.; Heine, T.; Kaiser, U.; Zhou, S.; Weitz, R. T.; Feng, X.; Dong, R. Interfacial synthesis of layer-oriented 2D conjugated metal-organic framework films toward directional charge transport. *J. Am. Chem. Soc.* **2021**, *143*, 13624−13632.
(65) Schultz, S. G.; Solomon, A. K. Determination of the effective hydrodynamic radii of small molecules by viscometry. *J. Gen. Physiol.* **1961**, *44*, 1189−1199.
(66) Ribeiro, A. C. F.; Valente, A. J. M.; Santos, C. I. A. V.; Prazeres, P. M. R. A.; Lobo, V. M. M.; Burrows, H. D.; Esteso, M. A.; Cabral, A. M. T. D. P. V.; Veiga, F. J. B. Binary mutual diffusion coefficients of aqueous solutions of α-cyclodextrin, 2-hydroxypropyl-α-cyclodextrin, and 2-hydroxypropyl-β-cyclodextrin at temperatures from (298.15 to 312.15) K. *J. Chem. Eng. Data* **2007**, *52*, 586−590.

https://doi.org/10.1021/acsnano.4c18135
ACS Nano 2025, 19, 12080−12089